The Astrophysical Journal Supplement Series, 191:340–351, 2010 December doi:10.1088/0067-0049/191/2/340
© 2010. The American Astronomical Society. All rights reserved. Printed in the U.S.A.

SOUTHERN COSMOLOGY SURVEY. II. MASSIVE OPTICALLY SELECTED CLUSTERS FROM 70 SQUARE DEGREES OF THE SUNYAEV–ZEL'DOVICH EFFECT COMMON SURVEY AREA

Felipe Menanteau[1], John P. Hughes[1], L. Felipe Barrientos[2], Amruta J. Deshpande[1], Matt Hilton[3], Leopoldo Infante[2], Raul Jimenez[4], Arthur Kosowsky[5], Kavilan Moodley[3], David Spergel[6], and Licia Verde[4]
[1] Department of Physics and Astronomy, Rutgers University, 136 Frelinghuysen Road, Piscataway, NJ 08854-8019, USA
[2] Departamento de Astronomía, Pontificia Universidad Católica de Chile, Santiago, Chile
[3] Astrophysics and Cosmology Research Unit, School of Mathematical Sciences, University of KwaZulu-Natal, Durban 4041, South Africa
[4] ICREA and Institute for Sciences of the Cosmos (ICC), University of Barcelona, Marti i Franques 1, Barcelona 08034, Spain
[5] Physics and Astronomy Department, University of Pittsburgh, 100 Allen Hall, 3941 O'Hara Street, Pittsburgh, PA 15260, USA
[6] Department of Astrophysical Sciences, Peyton Hall, Princeton University, Princeton, NJ 08544, USA
Received 2010 February 11; accepted 2010 October 23; published 2010 November 30

ABSTRACT

We present a catalog of 105 rich and massive ($M > 3 \times 10^{14}\ M_{\odot}$) optically selected clusters of galaxies extracted from 70 deg^2 of public archival *griz* imaging from the Blanco 4 m telescope acquired over 45 nights between 2005 and 2007. We use the clusters' optically derived properties to estimate photometric redshifts, optical luminosities, richness, and masses. We complement the optical measurements with archival *XMM-Newton* and *ROSAT* X-ray data which provide additional luminosity and mass constraints on a modest fraction of the cluster sample. Two of our clusters show clear evidence for central lensing arcs; one of these has a spectacular large diameter, nearly complete Einstein Ring surrounding the brightest cluster galaxy. A strong motivation for this study is to identify the massive clusters that are expected to display prominent signals from the Sunyaev–Zel'dovich effect (SZE) and therefore be detected in the wide-area millimeter-band surveys being conducted by both the Atacama Cosmology Telescope and the South Pole Telescope. The optical sample presented here will be useful for verifying new SZE cluster candidates from these surveys, for testing the cluster selection function, and for stacking analyses of the SZE data.

Key words: cosmic background radiation – cosmology: observations – galaxies: clusters: general – galaxies: distances and redshifts – large-scale structure of universe

Online-only material: color figures

1. INTRODUCTION

A new era of galaxy cluster surveys, based on measuring distortions in the cosmic microwave background (CMB), has begun. These distortions, known as the Sunyaev–Zel'dovich effect (SZE; Sunyaev & Zel'dovich 1972), have been detected for the first time in untargeted surveys over large areas of the sky by two new millimeter-band experiments: the Atacama Cosmology Telescope (ACT) and the South Pole Telescope (SPT). First results from ACT (Hincks et al. 2009) and SPT (Staniszewski et al. 2009) offer a taste of the future potential these experiments hold for obtaining large samples of essentially mass-selected clusters to arbitrary redshifts and have also provided the first measurement of the microwave background at arcminute angular scales (Lueker et al. 2010; Fowler et al. 2010).

Both ACT and SPT aim to provide unique samples of massive clusters of galaxies, selected by mass nearly independently of redshift, over a large area of the southern sky. While the number density of SZE-selected clusters can be used as a potentially strong probe of dark energy—as well as for studies of cluster physics, it is crucial to understand the systematics of SZE surveys by comparing with cluster identification using independent methods before the new cluster samples can be effectively used. For example, the low amplitude of the SZ component in the high-l CMB power spectrum (Lueker et al. 2010) or stacked clusters in the *Wilkinson Microwave Anisotropy Probe* (Komatsu et al. 2010) are recent issues that provide additional motivation for an independent search for clusters over the region being surveyed in the SZ. Furthermore, although the new millimeter-band telescopes can be used to identify clusters, coordinated optical data are necessary for confirmation and to determine redshifts and other fundamental properties of the new clusters.

The last decade has seen significant effort to produce large and well-selected optical catalogs of cluster of galaxies that can be used in cosmological, large-scale structure and galaxy evolution studies. The first systematic attempts to generate large samples of clusters, and to define their richness, came from the Abell catalogs (Abell 1958; Abell et al. 1989) which searched for projected galaxy overdensities through visual inspection of photographic plates successfully identifying thousands of clusters. Although optical catalogs can be relatively inexpensive and efficient at detecting low mass systems, early attempts were known to suffer from significant projection effects along the line of sight. The advent of CCD cameras and the digitization of large photographic plates has enabled the development of new search algorithms for galaxy clusters using a combination of space, brightness, and color information (i.e., photometric redshifts), minimizing projection issues (see Gal 2008, for a historical review of search methods). Among these algorithms are the pioneering implementation of a spatial matched filter technique (Postman et al. 1996) and its variants (Dong et al. 2008), the adaptive kernel technique (Gal et al. 2000, 2009), Voronoi tessellation (Ramella et al. 2001; Lopes et al. 2004), and methods exploiting the tight ridgeline in color–magnitude space of galaxies in clusters (Bower et al. 1992; Blakeslee et al. 2003) such as the red cluster sequence (RCS; Gladders & Yee 2000) and the MaxBCG (Annis et al. 1999; Koester et al. 2007a) techniques. This new wave of studies has produced large

sets of well-defined optical cluster catalogs covering thousands of square degrees (i.e., Goto et al. 2002; Gladders & Yee 2005; Koester et al. 2007b; Gal et al. 2009) providing reliable richness–mass correlations (Becker et al. 2007; Johnston et al. 2007; Reyes et al. 2008; Sheldon et al. 2009) and establishing independent cosmological constraints (Rozo et al. 2010) using optical catalogs.

In this article, we present new results from the Southern Cosmology Survey (SCS), our on-going multi-wavelength survey coordinated with ACT. Our first paper in this series, Menanteau et al. (2009), described our SCS imaging pipeline and presented a sample of new galaxy clusters from an 8 deg^2 optical imaging survey of the southern sky acquired at the Blanco 4 m telescope. Here, we complete our cluster analysis using all the 70 deg^2 contiguous imaging available, which represents a comoving volume of 0.076 Gpc^3 at $z = 0.6$. Throughout this paper, we assume a flat cosmology with $H_0 = 100h$ km s^{-1} Mpc^{-1}, $h = 0.7$ and matter density $\Omega_M = 0.3$.

2. DATA SET AND ANALYSIS

Our cluster analysis is based on all of the public unprocessed imaging data available for download at the time of writing from the observations carried out for the Blanco Cosmology Survey[7] (BCS) proposal. This was a NOAO Large Survey project (05B-0043, PI: Joe Mohr) that was awarded 45 nights between 2005 and 2007 to carry out intermediate depth g, r, i, z-band observations on the Cerro Tololo Inter-American Observatory (CTIO) Blanco 4 m telescope using the 8192 × 8192 pixel (0.36 deg^2) MOSAIC-II camera. The survey originally aimed to target two square 50 deg^2 southern sky patches centered near declinations -55° and -52° at right ascensions of 23 hr and 5 hr, respectively, that were to be contained in a larger SZE common region that both ACT and SPT would survey. After three years of observations the survey acquired 78 and 118 MOSAIC-II contiguous pointings at 23 hr and 5 hr, respectively, that correspond to 29 deg^2 and 41 deg^2 over each patch reaching a total of 70 deg^2 imaged in all *griz* filters. The pointing layout and the sky area covered for each patch are shown in Figure 1. The survey was awarded 15 extra nights at the end of 2008 to complete the proposed 100 deg^2; our analysis does not include this extra year's worth of observations as the data are not publicly available yet.

2.1. Data Processing

The raw unprocessed images were downloaded from the National Virtual Observatory[8] portal and were processed following the same procedures as described in our initial analysis (Menanteau et al. 2009) where we provide a full description of the data analysis followed and associated data products. Here, we briefly outline the steps involved and recent improvements from our original analysis. Our pipeline automatically handles the file associations and all of the initial standard CCD imaging tasks for each night's run as well as the secondary calibration steps (i.e., skyflats, fringe correction, cosmic-ray rejection, badpixel masks, world coordinate calibration, etc.) using a custom modified version of IRAF[9]/`mscred` (Valdes 1998). When observed, photometric standards from the Southern Hemisphere Standards

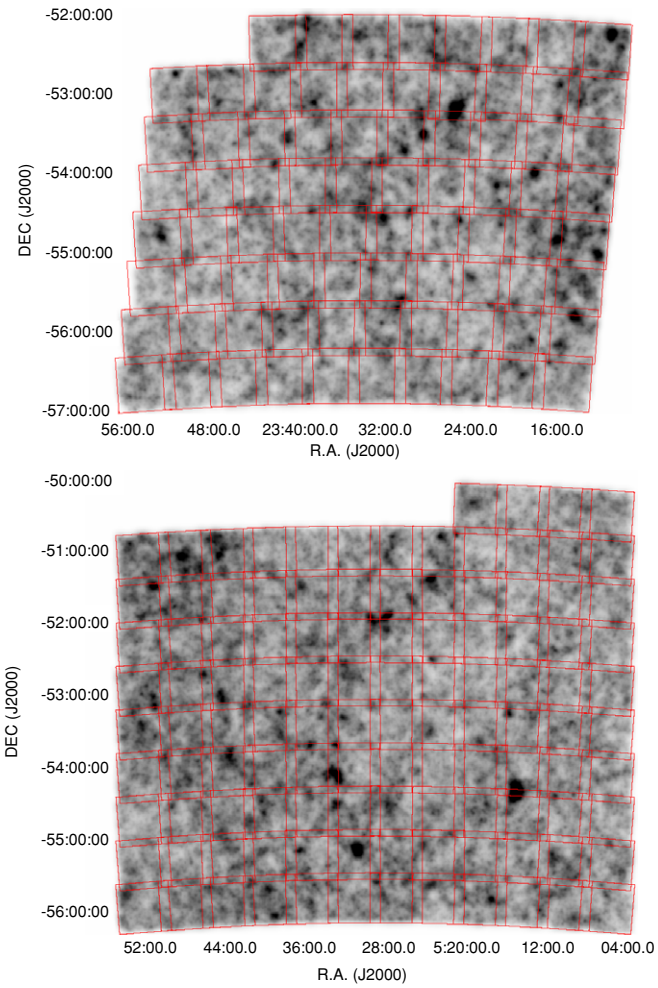

Figure 1. Computed likelihood density map images centered at $z = 0.3$ and width $\Delta z = 0.1$ over the 23 hr (top panel) and the 5 hr (bottom panel) field. Dark regions in the image represent denser areas. In red we show the area covered by each of the 78 and 112 MOSAIC-II tiles at 23 hr and 5 hr, respectively, that comprise the area studied over three years of observations.

(A color version of this figure is available in the online journal.)

Stars Catalog (Smith et al. 2007) were processed by the pipeline and a photometric zero point was estimated in AB magnitudes. Hereafter all magnitudes quoted are in the AB system. In Table 1, we show the observing dates, photometric conditions, and observed bands that comprise the data set we analyzed and that were used for this paper. We note that the information that went into creating this table was extracted from the raw data and header information of the data files.

In general each MOSAIC II pointing consisted of exposures of 2 × 125 s, 2 × 300 s, 3 × 450 s, and 3 × 235 s in the g, r, i and z-bands, respectively, with offsets of 3–5 arcmin (within each filter). We adjusted the photometric zero points of non-photometric nights using the overlapping regions between tiles and their matched sources from adjacent photometric tiles providing a homogeneous photometric calibration across each region with typical variations below 0.03 mag. The 2007 season data at 23 hr were particularly hard to match due to poor observing conditions and large variations within the individual exposures in each tile. We tackled this problem by first scaling all individual exposures comprising a tile to a common median scale; this step ensured that opposed edges of a combined frame could be effectively used to photometrically tie down adjacent tiles. This is a new feature of the pipeline.

[7] http://cosmology.uiuc.edu/BCS/

[8] http://portal-nvo.noao.edu

[9] IRAF is distributed by the National Optical Astronomy Observatory, which is operated by the Association of Universities for Research in Astronomy, Inc., under cooperative agreement with the National Science Foundation.

Table 1
2005–2007 Observations in the 23 hr and 5 hr Fields

Date	Photometric	No. of Tiles Obs 05 hr				No. of Tiles Obs 23 hr			
		g	*r*	*i*	*z*	*g*	*r*	*i*	*z*
2005 Nov 18	Yes	...	...	1.7	1.3	1.0	1.0	3.0	3.0
2005 Nov 19	Yes	...	...	4.7	5.0	4.5	4.5	1.0	1.0
2005 Nov 20	No	...	...	5.7	5.7	8.5	8.0	...	...
2005 Nov 22	No	...	...	...	...	...	...	...	...
2005 Nov 24	Yes	9.0	9.0	1.7	1.7	5.5	5.5	...	...
2005 Nov 26	Yes	9.5	9.0	1.0	1.0	4.5	4.5	1.0	1.0
2005 Nov 28	Yes	4.0	3.0	4.0	4.0	...	...	2.7	2.7
2005 Nov 30	Yes	12.5	12.5	...	...	5.0	5.0	0.3	0.3
2005 Dec 2	Yes	...	...	...	...	3.5	3.5	...	...
2005 Dec 4	No	9.0	9.0	...	...	2.0	2.0	...	...
2005 Dec 05	No	2.5	2.0	2.7	2.7	2.0	2.0	1.3	1.7
2005 Dec 6	Yes	...	...	4.0	4.0	...	...	1.3	1.0
2005 Dec 8	Yes	...	...	4.0	4.0	...	...	2.3	2.7
2005 Dec 10	Yes	...	...	5.7	5.7	...	...	3.0	3.0
2005 Dec 11	Yes	...	...	4.3	4.3	...	...	3.0	3.3
2006 Oct 23	Yes	9.0	10.5	...	...	...	...	5.0	5.0
2006 Oct 25	No	...	...	...	...	...	...	...	...
2006 Oct 27	Yes	10.5	7.0	...	...	...	...	5.0	5.3
2006 Oct 28	No	...	...	...	...	...	...	5.3	5.0
2006 Oct 29	Yes	8.0	8.0	2.0	2.0	...	...	4.0	4.3
2006 Oct 30	Yes	...	...	...	...	...	...	5.0	5.3
2006 Oct 31	Yes	...	...	6.0	6.0	...	...	3.0	2.7
2006 Dec 12	Yes	...	...	3.0	1.7	...	...	...	...
2006 Dec 13	Yes	...	...	3.0	3.3	1.0	0.5	...	...
2006 Dec 14	No	...	...	2.7	2.7	...	...	...	...
2006 Dec 15	Yes	4.0	4.0	5.7	5.7	...	...	...	...
2006 Dec 16	No	...	...	4.0	3.7	...	...	...	...
2006 Dec 17	Yes	7.0	6.5	4.3	5.0	...	...	...	...
2006 Dec 18	Yes	8.0	8.5	...	...	...	...	...	...
2006 Dec 19	Yes	3.0	3.0	6.3	6.3	...	...	...	...
2006 Dec 20	Yes	...	...	4.0	4.0	...	...	...	...
2006 Dec 21	Yes	...	...	8.7	8.7	...	...	...	...
2006 Dec 22	Yes	3.5	3.5	2.3	2.0	...	...	...	...
2006 Dec 23	Yes	6.5	6.0	6.0	6.3	...	...	...	...
2007 Sep 11	Yes	2.5	3.0	2.3	2.7	4.5	5.0	3.3	4.0
2007 Sep 12	Yes	...	...	...	...	1.0	1.0	1.0	1.0
2007 Sep 13	Yes	...	...	...	...	1.5	1.0	1.3	1.3
2007 Sep 14	Yes	1.5	1.5	1.7	1.3	4.5	5.0	4.7	4.7
2007 Sep 15	No	2.0	2.0	0.7	1.3	2.5	2.5	1.0	1.0
2007 Sep 16	Yes	...	...	...	...	2.5	2.5	...	...
2007 Sep 17	Yes	1.0	...	...	...	...	...	2.0	1.7
2007 Sep 18	yes	...	...	2.3	2.0	3.0	2.5	7.0	6.7
2007 Sep 19	yes	...	...	...	...	...	...	4.7	5.0
2007 Oct 11	Yes	...	...	...	...	...	...	...	...
2007 Oct 12	No	...	...	...	...	...	...	...	...
2007 Oct 30	No	...	...	1.0	...	...	0.5	...	...
2007 Oct 31	No	...	...	...	...	...	...	...	...
2007 Nov 1	Yes	...	...	1.3	2.3	2.5	2.0	...	...
2007 Nov 2	Yes	...	...	...	...	5.0	5.0	...	...
2007 Nov 3	Yes	...	...	3.0	3.0	9.5	9.5	...	...
2007 Nov 4	Yes	5.0	5.5	...	...	3.0	3.0	...	...
2007 Nov 6	Yes	...	...	...	...	...	...	4.7	4.3
2007 Nov 7	Yes	1.0	2.0	0.7	0.7	1.0	1.0	1.7	2.0
2007 Nov 8	Yes	...	...	...	...	...	...	...	...

Notes. Observing conditions during the 2005–2007 runs of the BCS as well as the number of tiles observed on each night. We only show the dates in which tiles in the 23 hr or 5 hr contiguous regions were observed.

All science images were mosaicked, aligned, and median combined using SWarp (Bertin 2006) to a plate scale of $0\farcs266$ pixel^{-1}. Source detection and photometry measurements for the science catalogs were performed using SExtractor (Bertin & Arnouts 1996). Large variations in the Galactic dust absorption on the 5 hr field led us to implement dust correction for every source in each observed band in the science catalogs utilizing the infrared maps and C-routines provided by Schlegel et al. (1998). This is particularly important to obtain unbiased colors for photometric redshifts. In Figure 2, we

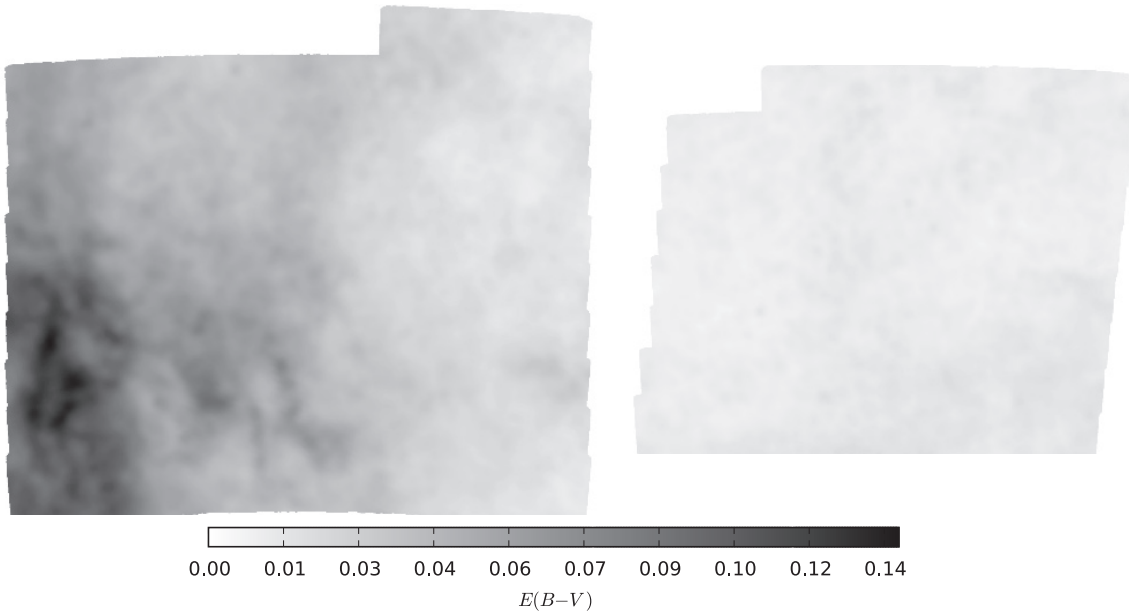

Figure 2. $E(B-V)$ dust extinction maps created for the 5 hr (left) and 23 hr (right) fields in magnitudes using the Schlegel et al. (1998) maps of dust infrared emission. Both maps are shown with the same $E(B-V)$ scale and size scales. Darker regions represent areas of higher Galactic dust absorption.

show our custom generated $E(B-V)$ Galactic dust absorption maps for the 5 hr and 23 hr regions, where darker regions represent areas of higher obscuration. From this figure, we can see that in the 23 hr region foreground Galactic absorption is negligible, while at 5 hr it can be as high as $E(B-V) \simeq 0.14$ mag. Finally, we determine photometric redshifts from the four-band optical images and the Galactic–extinction–corrected magnitudes using the Bayesian photometric redshift (BPZ; Benítez 2000) following the same procedure as discussed in Menanteau et al. (2009).

2.2. *Finding Clusters and Defining Membership*

In this section, we describe our efforts to select clusters of galaxies from multi-wavelength optical imaging. To this objective, we follow an identical procedure as the one we laid out in Menanteau et al. (2009) as part of our initial study of 8 deg^2 using the 2005 observations at 23 hr. We refer the reader there for an expanded and formal description of the method as well as for simulations that address the contamination and completeness of the search method. Here, we expanded our procedure to the full 70 deg^2 of Blanco *griz* contiguous imaging. Our cluster search algorithm uses a matched filter approach based on the one described in Postman et al. (1996) to identify significant overdensities. We define membership and estimate richness for each peak in the overdensity maps using the MaxBCG prescription (Koester et al. 2007a). Our method folds in the contributions from (1) a cluster spatial profile filter function, (2) a luminosity weight, and (3) the BPZ redshift probability distribution from each source to generate likelihood density maps or a "filtered" galaxy catalog over the area covered by the survey as a function of redshift. We generate likelihood density maps with a constant pixel scale of 1.2 arcmin at $\Delta z = 0.1$ intervals between $0.1 < z < 0.8$ over the surveyed regions. In Figure 1, we show an example of a likelihood density map centered at $z = 0.2$ on which we superpose outlines of the 78 and 112 tiles that define the 23 hr and 5 hr regions studied.

Because the mass of a cluster is not a direct observable, some observable proxy for mass needs to be used in order to obtain estimates for a given cluster sample. Such proxies include the X-ray flux and temperature (Reiprich & Böhringer 2002; Kravtsov et al. 2006; Rykoff et al. 2008; Rozo et al. 2009b; Vikhlinin et al. 2009), weak-lensing shear (Sheldon et al. 2009; Okabe et al. 2010), and optical galaxy richness of clusters (Becker et al. 2007; Rozo et al. 2009a). For this analysis, we use the latest mass tracers for clusters of galaxies that are based on optically observed parameters (Johnston et al. 2007; Reyes et al. 2008) extracted from a sample of around 13,000 clusters from the Sloan Digital Sky Survey (SDSS) MaxBCG catalog (Koester et al. 2007a). To use these mass tracers, we define membership in a similar fashion as Koester et al. (2007a). We then visually inspected each candidate-cluster peak in the density maps and selected the brightest elliptical galaxy in the cluster (BCG), which was taken to be the center and initial redshift of the system. We then use galaxies photometrically classified as E or E/S0s according to their BPZ spectral type and within a projected radius of $0.5h^{-1}$ Mpc and redshift interval $|z - z_o| = |\Delta z| = 0.05$ to obtain a local color–magnitude relation for each color combination as well as the cluster mean redshift, z_c, for all cluster members, using a 3σ median sigma-clipping algorithm. We use these to determine $N_{1\,\mathrm{Mpc}} = N_{\mathrm{gal}}$, the number of galaxies within $1h^{-1}$Mpc of the cluster center. For our richness measurements, we estimated the galaxy background contamination and implemented an appropriate background subtraction method following the same procedure as described in Menanteau et al. (2009; see Section 3.1). We use a statistical removal of unrelated field galaxies with similar colors and redshifts that were projected along the line of sight to each cluster. We estimate the surface number density of ellipticals in an annulus surrounding the cluster (within $R_{200} < r < 2R_{200}$) with $\Delta z = 0.05$ and the same colors as the cluster members. We measure this background contribution around the outskirts of each cluster and obtain a corrected value N_{gal} which is used to compute R_{200} and then corresponding values of N_{200}^{gal} and L_{200}. The magnitude of the correction ranges between 15% and 20%. We will refer to the corrected values hereafter.

Finally we show, as examples of the depth and data quality, composite *gri* color images of several clusters in the 5 hr and

Figure 3. Composite *gri* color image for nine newly discovered massive SCS clusters in the 5 hr field. We indicate the cluster's redshift using the median value from galaxy members within 250 kpc of the cluster's center.

23 hr regions in Figures 3 and 4, respectively, that cover a wide range of redshifts.

3. RESULTS

3.1. Optical Cluster Masses

The observational quantities required as input to the cluster mass scaling relation are $N_{200}^{\rm gal}$, L_{200}, and $L_{\rm BCG}$. The cluster richness, $N_{200}^{\rm gal}$, is the number of E and E/S0 galaxies within a given radius, originally defined by Hansen et al. (2005) as $R_{200} = 0.156 N_{1\,{\rm Mpc}}^{0.6} h^{-1}$ Mpc, with colors and luminosities that satisfy specific conditions for membership. Similarly, L_{200} is the total rest-frame integrated *r*-band luminosity, *k*-corrected to $z = 0.25$, of all member galaxies included in $N_{200}^{\rm gal}$, and $L_{\rm BCG}$ is the similarly defined rest-frame *r*-band luminosity of the BCG. Reyes et al. (2008) provide power-law functions for both the

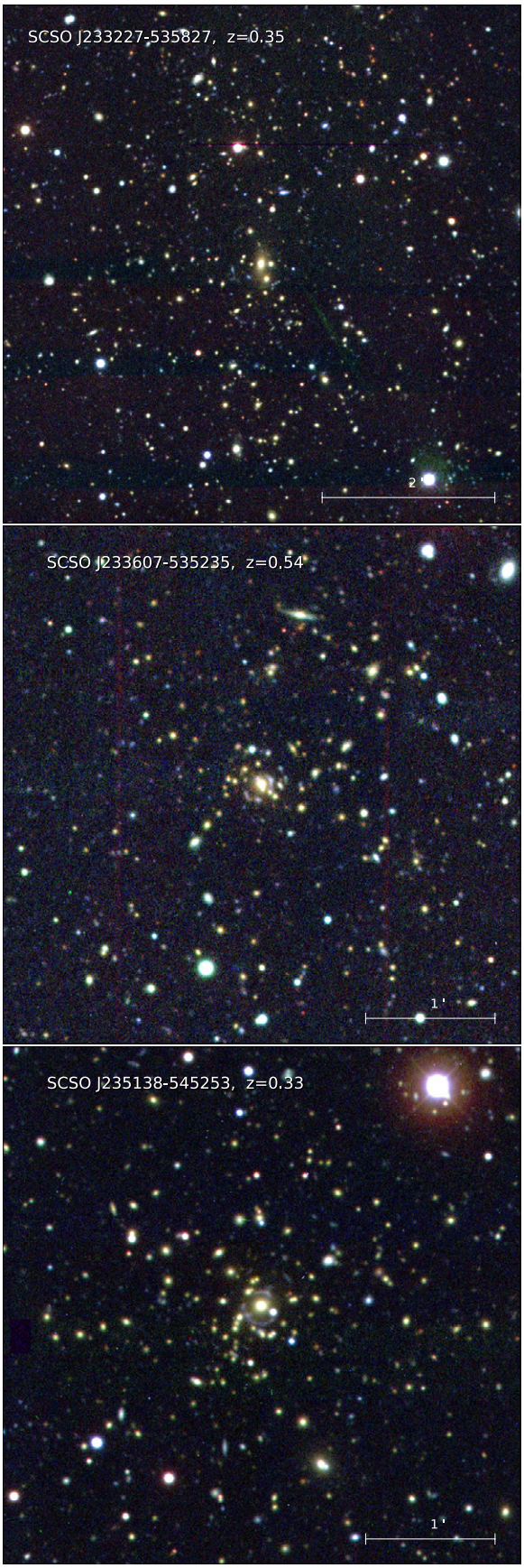

Figure 4. Composite *gri* color image for nine newly discovered massive SCS clusters in the 23 hr field. We indicate the cluster's redshift using the median value from galaxy members within 250 kpc of the cluster's center.

luminosity–mass and richness–mass relations (see Section 5.2.1 in their paper).

Both Johnston et al. (2007) and Reyes et al. (2008) found that the luminosity–mass and richness–mass relations were well described by power-law functions and they measured the normalizations and slopes in these relations using χ^2 minimization. We computed the two fitting functions based on L_{200} and $N_{200}^{\rm gal}$, (see Section 5.2.1 from Reyes et al. 2008 for full details), which are described as

$$M(N_{200}, L_{\rm BCG}) = M_N^0 (N_{200}/20)^{\alpha_N} \left(L_{\rm BCG}/\bar{L}_{\rm BCG}^{(N)}\right)^{\gamma_N} \quad (1)$$

and

$$M(L_{200}, L_{\rm BCG}) = M_L^0 (L_{200}/40)^{\alpha_L} \left(L_{\rm BCG}/\bar{L}_{\rm BCG}^{(L)}\right)^{\gamma_L}, \quad (2)$$

where M is the mass observational equivalent of $M_{200\bar{\rho}}$ (i.e., the halo mass enclosed within a radius of spherical volume within which the mean density is 200 times the average density) in units of $10^{14}\,M_\odot$, L_{200} is in units of $10^{10}h^{-2}\,L_\odot$, and the $L_{\rm BCG}$ dependence is normalized by its mean value. This is also described by a power-law function for a given value of L_{200} and $N_{200}^{\rm gal}$:

$$\bar{L}_{\rm BCG}^{(N)} \equiv \bar{L}_{\rm BCG}(N_{200}) = a_N N_{200}^{b_N} \quad (3)$$

and

$$\bar{L}_{\rm BCG}^{(L)} \equiv \bar{L}_{\rm BCG}(L_{200}) = a_L L_{200}^{b_L}. \quad (4)$$

The published best-fitting parameters for M^0, α, and γ in Equations (1) and (2) as well as the new erratum-corrected values of a and b (R. Reyes 2009, private communication) for Equations (3) and (4) are shown in Table 2. These recent changes in the values of the a and b parameters in Reyes et al. (2008) have implications for our mass estimation. Specifically, the changes translate into a decrease in mass when compared to our previous analysis of Menanteau et al. (2009) which used the initial parameters from their pre-print paper. As we discuss below, this change also affects the recovery of clusters in Menanteau et al. (2009) for the sky region that overlaps with this study.

We use this parameterization to obtain the optical mass estimates $M(N_{200})$ and $M(L_{200})$, based on $N_{200}^{\rm gal}$ and L_{200}, respectively, for all of the visually inspected clusters. Based on these estimates, we defined our catalog of massive clusters by selecting all systems with either $M(N_{200}) > 3 \times 10^{14}\,M_\odot$ or $M(L_{200}) > 3\times10^{14}\,M_\odot$ and $N_{\rm gal} > 10$. This defines the sample: 61 systems in the 5 hr region and 44 in the 23 hr region for a total of 105 clusters over 70 deg^2 of multi-band imaging. This mass threshold is aimed to include the upcoming $z < 0.8$ significant SZE detections from SPT and ACT. In Tables 3 and 4, we display the optical properties, photometric redshifts, positions, and mass estimates for all clusters at 23 hr and 5 hr, respectively. In these tables, we provide for each cluster the photometric redshift of the BCG as well as the mean photometric redshift for the system which was estimated using galaxies within 250 kpc of the BCG.

As we discussed in Menanteau & Hughes (2009), the expected luminosity range of BCGs in rich clusters has been already observationally established from the SDSS (Loh & Strauss 2006; Koester et al. 2007a) and it can be used as an additional probe to confirm the presence of a massive cluster. To this end in Figure 5 we compare the observed r-band magnitudes of all BCGs in our sample as a function of redshift to a parameterization of the observed r-band of SDSS BCGs (dashed curve). This corresponds to the $M^* - 1.5$ prescription from Loh & Strauss (2006) where we have used M^* from Blanton et al.

Table 2
Mass-richness Power-law Function Best Fitting Parameters from Reyes et al. (2008)

Redshift	$(10^{10}h^{-2}\,L_\odot)$									
	a_N	a_L	b_N	b_L	M_N^0	α_N	γ_N	M_L^0	α_L	γ_L
$0.10 < z < 0.23$	1.54	0.61	0.41	0.67	1.27 ± 0.08	1.20 ± 0.09	0.71 ± 0.14	1.81 ± 0.15	1.27 ± 0.17	0.40 ± 0.23
$0.23 < z < 0.70$	1.64	0.58	0.43	0.66	1.57 ± 0.14	1.12 ± 0.15	0.34 ± 0.24	1.76 ± 0.22	1.30 ± 0.29	0.26 ± 0.41

Table 3
Optical Clusters with $M(N_{200}) > 3 \times 10^{14}\,M_\odot$ or $M(L_{200}) > 3 \times 10^{14}\,M_\odot$ in the 23 hr Field

ID	$z_{\rm cluster}$	$z_{\rm BCG}$	$N_{\rm gal}$	$N_{200}^{\rm gal}$	$L_{200}[L_\odot]$	$M(N_{200})$ $(M_\odot)$	$M(L_{200})$
SCSO J231340−521919	0.21	0.21	61.2 ± 7.8	124.8 ± 11.2	$2.0 \times 10^{12} \pm 2.3 \times 10^{11}$	3.1×10^{14}	2.9×10^{14}
SCSO J231403−564710	0.60	0.60	22.7 ± 4.8	22.4 ± 4.7	$1.2 \times 10^{12} \pm 5.2 \times 10^{10}$	2.2×10^{14}	3.5×10^{14}
SCSO J231455−555308	0.21	0.23	59.6 ± 7.7	79.9 ± 8.9	$2.0 \times 10^{12} \pm 2.2 \times 10^{11}$	4.6×10^{14}	4.7×10^{14}
SCSO J231511−523322	0.36	0.39	29.0 ± 5.4	33.6 ± 5.8	$2.3 \times 10^{12} \pm 1.0 \times 10^{11}$	3.9×10^{14}	8.2×10^{14}
SCSO J231629−554535	0.51	0.53	33.9 ± 5.8	38.1 ± 6.2	$2.8 \times 10^{12} \pm 1.1 \times 10^{11}$	5.2×10^{14}	1.1×10^{15}
SCSO J231651−545356	0.36	0.36	35.5 ± 6.0	40.3 ± 6.3	$9.6 \times 10^{11} \pm 9.6 \times 10^{10}$	3.9×10^{14}	2.7×10^{14}
SCSO J231717−565723	0.74	0.73	21.0 ± 4.6	21.8 ± 4.7	$1.4 \times 10^{12} \pm 5.2 \times 10^{10}$	1.7×10^{14}	3.3×10^{14}
SCSO J231848−561711	0.51	0.51	28.8 ± 5.4	31.4 ± 5.6	$1.6 \times 10^{12} \pm 9.4 \times 10^{10}$	3.4×10^{14}	5.2×10^{14}
SCSO J231930−563858	0.36	0.37	35.4 ± 6.0	38.4 ± 6.2	$1.1 \times 10^{12} \pm 8.2 \times 10^{10}$	3.5×10^{14}	2.9×10^{14}
SCSO J232001−565222	0.80	0.80	18.0 ± 4.2	13.8 ± 3.7	$1.3 \times 10^{12} \pm 5.4 \times 10^{10}$	1.8×10^{14}	4.6×10^{14}
SCSO J232423−565705	0.75	0.75	25.0 ± 5.0	30.6 ± 5.5	$2.5 \times 10^{12} \pm 8.0 \times 10^{10}$	2.3×10^{14}	6.5×10^{14}
SCSO J232437−530047	0.73	0.75	38.7 ± 6.2	63.9 ± 8.0	$2.2 \times 10^{12} \pm 2.1 \times 10^{11}$	3.9×10^{14}	4.7×10^{14}
SCSO J232529−532420	0.74	0.71	40.8 ± 6.4	46.5 ± 6.8	$2.2 \times 10^{12} \pm 2.3 \times 10^{11}$	2.6×10^{14}	4.5×10^{14}
SCSO J232612−531858	0.15	0.13	77.2 ± 8.8	69.4 ± 8.3	$1.8 \times 10^{12} \pm 3.2 \times 10^{11}$	2.5×10^{14}	3.1×10^{14}
SCSO J232627−531512	0.74	0.74	39.2 ± 6.3	42.0 ± 6.5	$2.5 \times 10^{12} \pm 2.3 \times 10^{11}$	3.2×10^{14}	6.6×10^{14}
SCSO J232637−533911	0.76	0.77	34.4 ± 5.9	56.1 ± 7.5	$3.1 \times 10^{12} \pm 2.2 \times 10^{11}$	4.5×10^{14}	8.6×10^{14}
SCSO J232653−524149	0.11	0.11	52.8 ± 7.3	87.1 ± 9.3	$1.2 \times 10^{12} \pm 1.8 \times 10^{11}$	3.1×10^{14}	2.2×10^{14}
SCSO J232724−533553	0.74	0.74	56.6 ± 7.5	103.1 ± 10.2	$6.0 \times 10^{12} \pm 5.4 \times 10^{11}$	9.2×10^{14}	2.0×10^{15}
SCSO J232800−535152	0.74	0.75	36.8 ± 6.1	63.9 ± 8.0	$1.4 \times 10^{12} \pm 2.0 \times 10^{11}$	3.7×10^{14}	2.8×10^{14}
SCSO J232811−533847	0.74	0.74	43.1 ± 6.6	47.2 ± 6.9	$2.1 \times 10^{12} \pm 2.3 \times 10^{11}$	3.4×10^{14}	5.2×10^{14}
SCSO J232825−522814	0.73	0.70	35.0 ± 5.9	47.3 ± 6.9	$2.9 \times 10^{12} \pm 1.4 \times 10^{11}$	4.3×10^{14}	9.0×10^{14}
SCSO J232827−531414	0.36	0.35	34.7 ± 5.9	39.5 ± 6.3	$1.5 \times 10^{12} \pm 1.1 \times 10^{11}$	3.0×10^{14}	3.7×10^{14}
SCSO J232856−552428	0.57	0.57	20.3 ± 4.5	19.6 ± 4.4	$1.2 \times 10^{12} \pm 5.2 \times 10^{10}$	2.0×10^{14}	3.5×10^{14}
SCSO J232916−522910	0.73	0.74	39.8 ± 6.3	58.1 ± 7.6	$3.3 \times 10^{12} \pm 1.6 \times 10^{11}$	4.5×10^{14}	9.2×10^{14}
SCSO J233006−524035	0.73	0.71	36.4 ± 6.0	43.8 ± 6.6	$2.0 \times 10^{12} \pm 1.4 \times 10^{11}$	3.2×10^{14}	5.0×10^{14}
SCSO J233227−535827	0.35	0.32	41.0 ± 6.4	42.4 ± 6.5	$9.3 \times 10^{11} \pm 9.0 \times 10^{10}$	3.7×10^{14}	2.4×10^{14}
SCSO J233232−522016	0.36	0.37	37.4 ± 6.1	43.2 ± 6.6	$8.9 \times 10^{11} \pm 8.2 \times 10^{10}$	4.0×10^{14}	2.4×10^{14}
SCSO J233329−521513	0.51	0.50	36.8 ± 6.1	42.2 ± 6.5	$1.7 \times 10^{12} \pm 1.0 \times 10^{11}$	3.6×10^{14}	4.6×10^{14}
SCSO J233420−542732	0.56	0.55	31.7 ± 5.6	37.5 ± 6.1	$1.5 \times 10^{12} \pm 9.8 \times 10^{10}$	2.7×10^{14}	3.6×10^{14}
SCSO J233544−535115	0.51	0.51	58.8 ± 7.7	96.8 ± 9.8	$4.3 \times 10^{12} \pm 2.1 \times 10^{11}$	8.1×10^{14}	1.3×10^{15}
SCSO J233556−560602	0.64	0.63	14.2 ± 3.8	19.8 ± 4.5	$1.3 \times 10^{12} \pm 7.3 \times 10^{10}$	2.5×10^{14}	4.7×10^{14}
SCSO J233607−535235	0.54	0.53	60.1 ± 7.8	83.3 ± 9.1	$5.3 \times 10^{12} \pm 2.6 \times 10^{11}$	1.0×10^{15}	2.2×10^{15}
SCSO J233726−565655	0.50	0.52	26.7 ± 5.2	31.1 ± 5.6	$1.2 \times 10^{12} \pm 7.6 \times 10^{10}$	2.7×10^{14}	3.0×10^{14}
SCSO J233807−531223	0.47	0.49	46.1 ± 6.8	53.3 ± 7.3	$2.1 \times 10^{12} \pm 1.8 \times 10^{11}$	4.8×10^{14}	6.2×10^{14}
SCSO J233931−544525	0.73	0.71	29.6 ± 5.4	33.6 ± 5.8	$1.6 \times 10^{12} \pm 1.1 \times 10^{11}$	2.7×10^{14}	4.1×10^{14}
SCSO J234012−541907	0.59	0.62	25.9 ± 5.1	26.2 ± 5.1	$1.5 \times 10^{12} \pm 9.8 \times 10^{10}$	2.6×10^{14}	4.4×10^{14}
SCSO J234138−545210	0.55	0.56	25.7 ± 5.1	26.3 ± 5.1	$1.1 \times 10^{12} \pm 7.8 \times 10^{10}$	2.8×10^{14}	3.5×10^{14}
SCSO J234156−530848	0.49	0.49	44.7 ± 6.7	77.1 ± 8.8	$2.7 \times 10^{12} \pm 1.7 \times 10^{11}$	7.8×10^{14}	8.9×10^{14}
SCSO J234703−535051	0.56	0.55	21.6 ± 4.7	22.0 ± 4.7	$1.1 \times 10^{12} \pm 5.6 \times 10^{10}$	2.0×10^{14}	3.0×10^{14}
SCSO J234917−545521	0.73	0.72	17.9 ± 4.2	17.4 ± 4.2	$1.1 \times 10^{12} \pm 6.7 \times 10^{10}$	1.8×10^{14}	3.2×10^{14}
SCSO J235055−530124	0.46	0.48	41.4 ± 6.4	56.3 ± 7.5	$1.4 \times 10^{12} \pm 1.1 \times 10^{11}$	4.8×10^{14}	3.6×10^{14}
SCSO J235138−545253	0.33	0.31	71.4 ± 8.4	122.3 ± 11.1	$2.5 \times 10^{12} \pm 2.3 \times 10^{11}$	1.1×10^{15}	7.4×10^{14}
SCSO J235233−564348	0.74	0.72	17.1 ± 4.1	16.2 ± 4.0	$1.1 \times 10^{12} \pm 5.2 \times 10^{10}$	1.7×10^{14}	3.1×10^{14}
SCSO J235454−563311	0.51	0.50	33.1 ± 5.8	39.4 ± 6.3	$1.7 \times 10^{12} \pm 8.0 \times 10^{10}$	3.8×10^{14}	5.0×10^{14}

Notes. Catalog with the optical properties of clusters with mass estimates $>3 \times 10^{14}\,M_\odot$ in the 23 hr region. For each cluster, we note the BCG photometric redshift and the median photometric redshift for the clusters using the members within 250 kpc of the center of the cluster. The ID is based on the position of the BCG.

(2003) and allowed it to evolve passively with redshift. We see in the figure that all of the sources lie very close or well below (i.e., are intrinsically brighter) than the model curve as we would expect for the BCG in a rich cluster.

In our previous study (Menanteau et al. 2009), we presented a similar cluster analysis and mass estimation over 8 deg^2 area in the 23 hr region which is fully contained in the current 70 deg^2 data set. However, due to the changes in the mass parameterization prescription we did not recover all the massive clusters from Menanteau et al. (2009) even though the nominal mass threshold was the same ($M > 3 \times 10^{14}\,M_\odot$) as here. Therefore, only three out of eight clusters from Table 5 of

Table 4
Optical Clusters with $M(N_{200}) > 3 \times 10^{14}\,M_\odot$ or $M(L_{200}) > 3 \times 10^{14}\,M_\odot$ in the 5 hr Field

ID	$z_{\rm cluster}$	$z_{\rm BCG}$	$N_{\rm gal}$	$N_{200}^{\rm gal}$	$L_{200}(L_\odot)$	$M(N_{200})$	$M(L_{200})$
						($M_\odot$)	
SCSO J050854−513048	0.70	0.70	25.0 ± 5.0	23.9 ± 4.9	$1.3 \times 10^{12} \pm 1.4 \times 10^{11}$	2.4×10^{14}	3.8×10^{14}
SCSO J050857−535837	0.76	0.78	37.0 ± 6.1	48.5 ± 7.0	$3.5 \times 10^{12} \pm 2.4 \times 10^{11}$	5.0×10^{14}	1.2×10^{15}
SCSO J050902−520704	0.58	0.58	35.3 ± 5.9	37.0 ± 6.1	$1.9 \times 10^{12} \pm 1.7 \times 10^{11}$	2.8×10^{14}	4.8×10^{14}
SCSO J050926−522227	0.67	0.70	30.9 ± 5.6	33.5 ± 5.8	$1.6 \times 10^{12} \pm 1.8 \times 10^{11}$	2.5×10^{14}	4.0×10^{14}
SCSO J051023−544455	0.39	0.37	45.2 ± 6.7	51.0 ± 7.1	$1.1 \times 10^{12} \pm 1.7 \times 10^{11}$	3.5×10^{14}	2.3×10^{14}
SCSO J051112−523112	0.73	0.73	31.7 ± 5.6	34.4 ± 5.9	$2.2 \times 10^{12} \pm 2.2 \times 10^{11}$	3.3×10^{14}	6.6×10^{14}
SCSO J051136−561045	0.70	0.71	30.9 ± 5.6	35.0 ± 5.9	$2.9 \times 10^{12} \pm 1.6 \times 10^{11}$	3.2×10^{14}	8.7×10^{14}
SCSO J051144−511416	0.48	0.48	33.3 ± 5.8	40.1 ± 6.3	$1.6 \times 10^{12} \pm 1.8 \times 10^{11}$	2.9×10^{14}	3.7×10^{14}
SCSO J051145−515430	0.70	0.70	32.7 ± 5.7	32.4 ± 5.7	$1.6 \times 10^{12} \pm 2.1 \times 10^{11}$	2.2×10^{14}	3.5×10^{14}
SCSO J051207−514204	0.48	0.46	37.7 ± 6.1	49.1 ± 7.0	$1.6 \times 10^{12} \pm 1.9 \times 10^{11}$	3.5×10^{14}	3.9×10^{14}
SCSO J051225−505913	0.70	0.70	49.8 ± 7.0	54.6 ± 7.4	$3.0 \times 10^{12} \pm 3.2 \times 10^{11}$	4.9×10^{14}	9.2×10^{14}
SCSO J051240−513941	0.66	0.66	33.8 ± 5.8	30.8 ± 5.5	$1.5 \times 10^{12} \pm 1.9 \times 10^{11}$	2.2×10^{14}	3.5×10^{14}
SCSO J051245−502028	0.62	0.62	24.2 ± 4.9	23.3 ± 4.8	$2.6 \times 10^{12} \pm 5.4 \times 10^{10}$	2.8×10^{14}	9.4×10^{14}
SCSO J051258−542153	0.67	0.68	18.5 ± 4.3	18.4 ± 4.3	$1.3 \times 10^{12} \pm 1.2 \times 10^{11}$	2.0×10^{14}	4.0×10^{14}
SCSO J051400−512635	0.72	0.73	54.7 ± 7.4	81.7 ± 9.0	$5.7 \times 10^{12} \pm 4.9 \times 10^{11}$	7.0×10^{14}	1.8×10^{15}
SCSO J051412−514004	0.67	0.66	44.8 ± 6.7	60.9 ± 7.8	$2.5 \times 10^{12} \pm 3.1 \times 10^{11}$	4.2×10^{14}	6.0×10^{14}
SCSO J051457−514345	0.69	0.69	36.4 ± 6.0	37.4 ± 6.1	$4.0 \times 10^{12} \pm 3.4 \times 10^{11}$	4.1×10^{14}	1.5×10^{15}
SCSO J051542−514017	0.73	0.73	40.4 ± 6.3	53.4 ± 7.3	$2.4 \times 10^{12} \pm 3.3 \times 10^{11}$	4.0×10^{14}	6.3×10^{14}
SCSO J051558−543906	0.66	0.64	33.7 ± 5.8	38.4 ± 6.2	$1.5 \times 10^{12} \pm 1.8 \times 10^{11}$	2.8×10^{14}	3.5×10^{14}
SCSO J051613−542620	0.38	0.36	45.9 ± 6.8	65.2 ± 8.1	$4.3 \times 10^{12} \pm 2.4 \times 10^{11}$	6.8×10^{14}	1.5×10^{15}
SCSO J051637−543001	0.23	0.25	127.0 ± 11.3	180.3 ± 13.4	$5.3 \times 10^{12} \pm 1.0 \times 10^{12}$	1.8×10^{15}	1.9×10^{15}
SCSO J051755−555727	0.66	0.66	20.4 ± 4.5	18.2 ± 4.3	$1.2 \times 10^{12} \pm 1.1 \times 10^{11}$	1.7×10^{14}	3.4×10^{14}
SCSO J051933−554243	0.69	0.70	25.0 ± 5.0	23.8 ± 4.9	$2.5 \times 10^{12} \pm 1.8 \times 10^{11}$	2.9×10^{14}	9.1×10^{14}
SCSO J051935−554916	0.75	0.75	25.8 ± 5.1	25.7 ± 5.1	$1.6 \times 10^{12} \pm 1.7 \times 10^{11}$	2.2×10^{14}	4.3×10^{14}
SCSO J052051−561804	0.74	0.73	55.4 ± 7.5	91.0 ± 9.5	$4.5 \times 10^{12} \pm 3.7 \times 10^{11}$	7.1×10^{14}	1.3×10^{15}
SCSO J052113−510418	0.64	0.61	58.2 ± 7.6	85.1 ± 9.2	$4.8 \times 10^{12} \pm 4.9 \times 10^{11}$	7.9×10^{14}	1.6×10^{15}
SCSO J052200−502700	0.50	0.47	74.0 ± 8.6	133.7 ± 11.6	$4.1 \times 10^{12} \pm 4.0 \times 10^{11}$	9.4×10^{14}	1.1×10^{15}
SCSO J052533−551818	0.72	0.72	19.1 ± 4.4	15.3 ± 3.9	$1.6 \times 10^{12} \pm 1.4 \times 10^{11}$	1.5×10^{14}	4.8×10^{14}
SCSO J052608−561114	0.14	0.15	41.6 ± 6.5	63.4 ± 8.0	$1.4 \times 10^{12} \pm 2.6 \times 10^{11}$	3.5×10^{14}	3.2×10^{14}
SCSO J052803−525945	0.68	0.69	61.5 ± 7.8	85.3 ± 9.2	$4.3 \times 10^{12} \pm 4.4 \times 10^{11}$	6.8×10^{14}	1.2×10^{15}
SCSO J052810−514839	0.65	0.64	24.6 ± 5.0	23.6 ± 4.8	$1.7 \times 10^{12} \pm 1.3 \times 10^{11}$	2.3×10^{14}	5.0×10^{14}
SCSO J052858−535744	0.70	0.70	37.4 ± 6.1	53.6 ± 7.3	$3.0 \times 10^{12} \pm 3.1 \times 10^{11}$	4.2×10^{14}	8.1×10^{14}
SCSO J052951−551611	0.66	0.65	26.7 ± 5.2	30.3 ± 5.5	$2.4 \times 10^{12} \pm 1.9 \times 10^{11}$	3.3×10^{14}	8.1×10^{14}
SCSO J053052−552056	0.73	0.71	40.8 ± 6.4	71.3 ± 8.4	$4.4 \times 10^{12} \pm 4.2 \times 10^{11}$	5.8×10^{14}	1.3×10^{15}
SCSO J053154−552031	0.23	0.21	92.3 ± 9.6	114.5 ± 10.7	$2.6 \times 10^{12} \pm 5.1 \times 10^{11}$	7.9×10^{14}	6.6×10^{14}
SCSO J053327−542016	0.23	0.25	47.7 ± 6.9	77.3 ± 8.8	$1.7 \times 10^{12} \pm 3.3 \times 10^{11}$	3.3×10^{14}	3.4×10^{14}
SCSO J053437−552312	0.76	0.80	15.4 ± 3.9	8.4 ± 2.9	$1.4 \times 10^{12} \pm 1.3 \times 10^{11}$	1.1×10^{14}	5.1×10^{14}
SCSO J053448−543534	0.65	0.65	23.0 ± 4.8	24.0 ± 4.9	$1.3 \times 10^{12} \pm 1.3 \times 10^{11}$	2.4×10^{14}	3.9×10^{14}
SCSO J053500−532018	0.59	0.57	23.1 ± 4.8	22.8 ± 4.8	$3.2 \times 10^{12} \pm 1.3 \times 10^{11}$	2.9×10^{14}	1.2×10^{15}
SCSO J053632−553123	0.72	0.72	54.5 ± 7.4	98.8 ± 9.9	$4.5 \times 10^{12} \pm 5.7 \times 10^{11}$	6.2×10^{14}	1.1×10^{15}
SCSO J053638−553854	0.74	0.71	40.7 ± 6.4	65.9 ± 8.1	$2.2 \times 10^{12} \pm 3.1 \times 10^{11}$	3.9×10^{14}	4.8×10^{14}
SCSO J053645−553302	0.74	0.71	37.1 ± 6.1	62.7 ± 7.9	$2.0 \times 10^{12} \pm 3.2 \times 10^{11}$	4.4×10^{14}	4.9×10^{14}
SCSO J053655−553809	0.76	0.72	41.8 ± 6.5	64.7 ± 8.1	$2.9 \times 10^{12} \pm 3.2 \times 10^{11}$	4.6×10^{14}	7.2×10^{14}
SCSO J053715−541530	0.49	0.51	21.1 ± 4.6	20.1 ± 4.5	$1.1 \times 10^{12} \pm 1.1 \times 10^{11}$	2.0×10^{14}	3.1×10^{14}
SCSO J053732−542521	0.62	0.61	21.5 ± 4.6	21.4 ± 4.6	$2.4 \times 10^{12} \pm 1.3 \times 10^{11}$	2.5×10^{14}	8.6×10^{14}
SCSO J053952−561423	0.36	0.36	36.9 ± 6.1	48.4 ± 7.0	$1.1 \times 10^{12} \pm 1.4 \times 10^{11}$	4.1×10^{14}	2.9×10^{14}
SCSO J054012−561700	0.38	0.38	51.4 ± 7.2	59.4 ± 7.7	$1.5 \times 10^{12} \pm 1.8 \times 10^{11}$	5.0×10^{14}	3.9×10^{14}
SCSO J054022−541622	0.51	0.48	35.1 ± 5.9	46.1 ± 6.8	$1.8 \times 10^{12} \pm 1.9 \times 10^{11}$	3.3×10^{14}	4.3×10^{14}
SCSO J054052−551943	0.76	0.78	40.9 ± 6.4	57.5 ± 7.6	$3.0 \times 10^{12} \pm 3.2 \times 10^{11}$	4.5×10^{14}	8.1×10^{14}
SCSO J054228−525002	0.65	0.66	21.8 ± 4.7	21.3 ± 4.6	$1.7 \times 10^{12} \pm 1.3 \times 10^{11}$	1.8×10^{14}	4.5×10^{14}
SCSO J054332−505651	0.35	0.36	45.5 ± 6.8	64.0 ± 8.0	$1.3 \times 10^{12} \pm 1.9 \times 10^{11}$	4.1×10^{14}	2.8×10^{14}
SCSO J054358−531349	0.24	0.25	30.0 ± 5.5	41.2 ± 6.4	$9.9 \times 10^{11} \pm 1.8 \times 10^{11}$	3.1×10^{14}	2.3×10^{14}
SCSO J054401−511254	0.28	0.28	31.4 ± 5.6	43.3 ± 6.6	$1.2 \times 10^{12} \pm 1.6 \times 10^{11}$	3.4×10^{14}	3.0×10^{14}
SCSO J054407−530924	0.25	0.26	42.9 ± 6.5	47.4 ± 6.9	$1.0 \times 10^{12} \pm 1.9 \times 10^{11}$	3.3×10^{14}	2.2×10^{14}
SCSO J054436−550319	0.35	0.36	33.0 ± 5.8	41.5 ± 6.4	$1.9 \times 10^{12} \pm 1.6 \times 10^{11}$	3.6×10^{14}	5.3×10^{14}
SCSO J054721−554906	0.59	0.59	38.1 ± 6.2	49.2 ± 7.0	$2.4 \times 10^{12} \pm 2.1 \times 10^{11}$	4.2×10^{14}	6.8×10^{14}
SCSO J054742−554836	0.50	0.50	26.6 ± 5.2	25.8 ± 5.1	$1.3 \times 10^{12} \pm 1.2 \times 10^{11}$	2.5×10^{14}	3.9×10^{14}
SCSO J054811−555601	0.64	0.64	27.4 ± 5.2	28.7 ± 5.3	$2.2 \times 10^{12} \pm 1.5 \times 10^{11}$	2.8×10^{14}	6.6×10^{14}
SCSO J054931−522655	0.38	0.39	21.2 ± 4.6	22.0 ± 4.7	$2.1 \times 10^{12} \pm 1.1 \times 10^{11}$	2.7×10^{14}	7.5×10^{14}
SCSO J054949−513503	0.28	0.28	38.4 ± 6.2	51.4 ± 7.2	$1.3 \times 10^{12} \pm 1.8 \times 10^{11}$	4.2×10^{14}	3.3×10^{14}
SCSO J055017−534601	0.49	0.47	30.8 ± 5.5	29.9 ± 5.5	$1.4 \times 10^{12} \pm 1.4 \times 10^{11}$	2.5×10^{14}	3.6×10^{14}

Notes. Catalog with the optical properties of clusters with mass estimates $>3 \times 10^{14}\,M_\odot$ in the 5 hr region. For each cluster, we note the BCG photometric redshift and the median photometric redshift for the clusters using the members within 250 kpc of the center of the cluster. The ID is based on the position of the BCG.

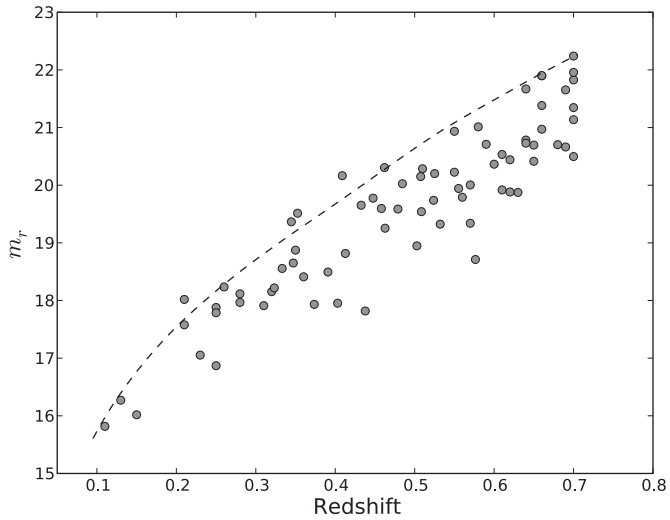

Figure 5. r-band observed magnitude for the BCGs in our sample as a function of the redshift of the cluster (filled circles). We also show the $M^* - 1.5$ BCG–redshift relationship from Loh & Strauss (2006) as the dashed curve.

Menanteau et al. (2009) are massive enough to appear in the current paper's Table 3, while the remaining clusters, although detected, now have masses that fall below the $3 \times 10^{14}\,M_\odot$ mass limit. Similarly, when comparing with the weak-lensing mass estimates of McInnes et al. (2009) we can only match the same three sources with clusters in their analysis (see Table 2 of their paper). On the other hand, there is now a better agreement between the updated $M(L_{200})$ values and the weak-lensing masses for the matched clusters.

3.2. Lensing Rate

Out of the 105 massive clusters in the sample we report two systems (see the two lower panels of Figure 4) with obvious evidence of arcs near the BCG. Of these two lensing clusters, SCSO 235138−545253 at $z = 0.33$ is a potentially unique system in that it shows a large diameter ($\sim 15''$), nearly complete Einstein Ring embedded in a massive cluster. Although our density of lensing clusters is not widely different from the Gladders et al. (2003) RCS sample of five lensing clusters over $\sim 90\,\mathrm{deg}^2$, all of the Gladders et al. clusters are at $z > 0.64$, while both of our systems are at $z < 0.54$ making them completely exclusive in redshift. Moreover, none of the Gladders et al. (2003) sample shows anything close to a complete Einstein Ring.

3.3. Correlation with Known Sources

We queried the NASA/IPCA Extragalactic Database (NED)[10] for cataloged clusters from *ROSAT*, Abell et al. (1989), ACT (Hincks et al. 2009), and SPT (Staniszewski et al. 2009; Menanteau & Hughes 2009) within a $3'$ radius of the location of each SCS cluster (see Table 5). In some cases, there was a cataloged galaxy from the Two Micron All Sky Survey (Skrutskie et al. 2006, NED ID: 2MASX), which we report if it is within $10''$ of the BCG. We also take note of radio sources within $1'$ of our cluster positions since these could potentially bias the cluster SZ signal. We only found radio sources from the Sydney University Molonglo Sky Survey (SUMSS) at 843 MHz (Mauch et al. 2003). Finally, we find one unidentified bright X-ray source from the *ROSAT* All Sky Survey (RASS; Voges et al. 1999) that is coincident with one of our clusters.

It is interesting to note that although we recover two of the SZE-selected clusters from the first SPT results (Staniszewski et al. 2009), there are two others from that study which we do not recover. One of these (SPT-CL 0509−5342) falls below the mass threshold used here with mass estimates of $2.1 \times 10^{14}\,M_\odot$ and $1.2 \times 10^{14}\,M_\odot$ for $M(N_{200})$ and $M(L_{200})$, respectively. These are lower than the optical mass quoted in Menanteau & Hughes (2009) due to the change in the Reyes et al. (2008) mass parameterization but are still comparable to the weak-lensing mass range, $(1.9\text{–}5.6) \times 10^{14}\,M_\odot$, obtained by McInnes et al. (2009) using the same optical data set. The other cluster (SPT-CL0547−5345) has a photometric redshift of 0.88 (Menanteau & Hughes 2009) that puts it beyond the redshift threshold ($z = 0.8$) we use here.

3.4. ROSAT Archival Data

We searched for X-ray counterparts to the SCS optical clusters using the RASS data following the same procedure as in Menanteau & Hughes (2009). The raw X-ray photon event lists and exposure maps were downloaded from the MPE *ROSAT* Archive[11] and queried with our own custom software. At the position of each SCS cluster, RASS count rates in the 0.5–2 keV band (corresponding to PI channels 52–201) were extracted from within a $3'$ radius for the source emission and from within a surrounding annulus ($5'$–$25'$ inner and outer radii) for the background emission. The background-subtracted count rates were converted to X-ray luminosity (in the 0.5–2.0 keV band) assuming a thermal spectrum ($kT = 5$ keV) and the Galactic column density of neutral hydrogen appropriate to the source position, using data from the Leiden/Argentine/HI Bonn survey (Kalberla et al. 2005). X-ray masses within an overdensity of 500 times the critical density were then determined using the L_X versus M_{500} scaling relation from Vikhlinin et al. (2009). These were then converted to an overdensity of 200 with respect to the average density of the universe for comparison to the optically derived masses using a simple multiplicative scaling factor of 1.77. This factor is good to 10% over the redshift and mass range of our sample. In Table 6 we show redshifts, column densities, rates, luminosities, and masses only for those clusters with X-ray emission significant at 2σ or higher, while Figure 6 shows all the SCS clusters with either actual values for the X-ray mass or (for most cases) upper limits. We also show points corresponding to a simple stacking of the X-ray and the optical masses for clusters in three redshift and three optical mass bins as the green and red dots, respectively. Each point represents an average of ~ 20 clusters each with some positive X-ray count rate, excluding the several higher significance individual cases plotted in the figure. It is encouraging that the points scatter by about a factor of two around the line of equal optical and X-ray masses, suggesting that the X-ray emission is in fact associated with hot gas in the potential well of a massive cluster. In at least two cases, we have recovered known clusters (SCSO J051637−543001 and SCSO J232653−524149). And two of the RASS-correlated clusters (SCSO J053154−552031 and SCSO J233227−535827) are among those shown in the color images (i.e., see the bottom left panel of Figure 3 and the top panel of Figure 4).

[10] http://nedwww.ipac.caltech.edu/

[11] ftp://ftp.xray.mpe.mpg.de/rosat/archive/

Table 5
Cataloged Sources Associated with SCS Optical Clusters

SCS ID	Catalog Name	Distance to BCG	Source Type
SCSO J051412−514004	SUMSS J051411−513953	13″	RadioS
SCSO J051637−543001	2MASX J05163736−5430017	3″	Galaxy
″	Abell S0520, RXC J0516.6−5430	2.′4	GClstr ($z = 0.2952$)
″	ACT-CL J0516−5432,SPT-CL 0517−5430	2.′8,0.′5	SZ-GClstr
SCSO J052113−510418	SUMSS J052114−510419	13″	RadioS
SCSO J052533−551818	Abell S0529	1.′5	GClstr
SCSO J052608−561114	Abell S0530	2.′4	GClstr
SCSO J052803−525945	SUMSS J052805−525953	24″	RadioS
″	SPT-CL 0528−5300	0.′4	SZ-GClstr
SCSO J053327−542016	2MASX J05332723−5420154	2″	Galaxy
SCSO J053437−552312	SUMSS J053442−552248	55″	RadioS
SCSO J053632−553123	SUMSS J053629−553147	30″	RadioS
SCSO J053715−541530	SUMSS J053718−541608	48″	RadioS
SCSO J054012−561700	SUMSS J054014−561723	31″	RadioS
SCSO J054407−530924	SUMSS J054406−530922	8″	RadioS
SCSO J054949−513503	SUMSS J054948−513454	9″	RadioS
SCSO J055017−534601	SUMSS J055019−534601	25″	RadioS
SCSO J231455−555308	2MASX J23145553−5553093	5″	Galaxy
SCSO J232001−565222	SUMSS J232001−565219	4″	RadioS
SCSO J232653−524149	RXC J2326.7−5242	1.′2	GClstr ($z = 0.1074$)
″	SUMSS J232654−524153	14″	RadioS
SCSO J233227−535827	1RXS J233224.3−535840	27″	XrayS
SCSO J233544−535115	SUMSS J233544−535113	3″	RadioS
SCSO J234156−530848	SUMSS J234156−530849	5″	RadioS
SCSO J234703−535051	SUMSS J234703−535052	3″	RadioS
SCSO J234917−545521	SUMSS J234917−545518	8″	RadioS
SCSO J235055−530124	SUMSS J235054−530141	17″	RadioS
SCSO J235138−545253	2MASX J23513813−5452538	2″	Galaxy
″	SUMSS J235138−545255	3″	RadioS

Note. Cataloged sources from the NASA/IPAC Extragalactic Database (NED) correlated with SCS optical clusters.

Table 6
Optical Clusters with X-ray Counterparts from the RASS

SCS ID	$z_{\rm cluster}$	$N_{\rm H}$ (10^{20} cm^{-2})	Rate (counts s^{-1})	L_X(0.5–2.0 keV) (10^{44} erg s^{-1})	$M_{200}(L_X)$ ($M_\odot$)
SCSO J051136−561045	0.70	1.61	0.015 ± 0.006	3.0 ± 1.3	7.9×10^{14}
SCSO J051637−543001	0.2952*	2.05	0.205 ± 0.030	6.1 ± 0.9	1.6×10^{15}
SCSO J052533−551818	0.72	4.08	0.011 ± 0.005	2.5 ± 1.2	6.9×10^{14}
SCSO J053154−552031	0.23	5.20	0.017 ± 0.006	0.3 ± 0.1	2.7×10^{14}
SCSO J053952−561423	0.36	4.90	0.010 ± 0.005	0.5 ± 0.3	3.3×10^{14}
SCSO J054407−530924	0.25	5.01	0.020 ± 0.005	0.5 ± 0.1	3.3×10^{14}
SCSO J054721−554906	0.59	6.98	0.007 ± 0.004	1.2 ± 0.6	4.8×10^{14}
SCSO J054949−513503	0.28	4.58	0.012 ± 0.004	0.3 ± 0.1	2.7×10^{14}
SCSO J232653−524149	0.1074*	1.28	0.166 ± 0.035	0.6 ± 0.1	4.1×10^{14}
SCSO J233227−535827	0.35	1.28	0.091 ± 0.026	3.9 ± 1.1	1.2×10^{15}

Notes. Catalog of the optical clusters associated with X-ray emission in the RASS. The quoted redshifts are just repeated from Tables 3 and 4 except for the starred values which are spectroscopic redshifts from NED (see Table 5). Rates were extracted from within 3′ radii circles except for the three brightest clusters, SCSO J051637−543001, SCSO J232653−524149, and SCSO J233227−535827, for which radii of 10′, 7′, and 6′, respectively, were used.

3.5. XMM-Newton Archival Data

There are a number of *XMM-Newton* pointings that overlap with the SCS especially in the 23 hr region. Table 7 lists all the optical clusters from this study (Tables 3 and 4) that are located within the field of view of an archival *XMM-Newton* pointing (specifically the following ObsIds: 0205330301, 0505380601, 0505381801, 0505382201, and 0505383601). In several cases, there is an associated X-ray source detected by the Pipeline Processing System (PPS) which is run on all *XMM-Newton* pointings to produce standard results and are provided to the observer. If a PPS source exists, we list its ID, the offset in arcseconds between the X-ray source and the optical cluster position and whether or not the PPS has flagged the X-ray source are being extended. To determine fluxes and luminosities, we extract spectra from circular regions chosen to maximize the extracted count rate for the extended X-ray sources. For the other sources we use a 1′ radius circle. Background spectra come from a surrounding annular region with sufficient area to obtain good photon statistics. The rate, summed over the single PN and both MOS detectors, is quoted in Column 7 of Table 7. We also used standard *XMM-Newton* software tools to calculate the

Table 7
Optical Clusters Located within the Field of View of *XMM-Newton* Observations

SCS ID	$z_{\rm cluster}$	$N_{\rm H}$ (10^{20} cm^{-2})	X-ray ID	Offset ($''$)	Extended	Extr Rad (kpc)	Rate[a] (0.5–2.0 keV)	L_X[b]	$M(L_X)$ (10^{14} $M_\odot$)
SCSO J051558−543906	0.64	2.07	XMM J051600−543900	19	Yes	910 (2.2′)	15.7 ± 2.6	0.60	3.0
SCSO J051613−542620	0.36	1.98	...	...	...	300 (1′)	6.8 ± 1.4	0.027	0.5
SCSO J051637−543001	0.2952*	2.05	XMM J051635−543022	25	Yes	1390 (5.3′)	1740 ± 15	5.1	14.4
SCSO J231651−545356	0.36	1.29	XMM J231653−545410	26	Yes	650 (2.2′)	73.7 ± 3.5	0.71	4.1
SCSO J232856−552428	0.57	1.29	XMM J232856−552429	5	No	390 (1′)	5.4 ± 1.3	0.07	0.8
SCSO J233420−542732	0.55	1.27	...	...	...	380 (1′)	5.2 ± 1.4	0.08	0.9
SCSO J233556−560602	0.63	1.27	...	...	...	410 (1′)	6.2 ± 1.7	0.10	1.0

Notes. Luminosities calculated by fitting an absorbed thermal emission model with a fixed 5 keV temperature, except for SCSO J051558−543906, SCSO J051637−543001, and SCSO J231651−545356 for which there was enough signal to determine their temperatures (see the text). The quoted redshifts are just repeated from Tables 3 and 4 except for the starred value which is a spectroscopic redshift from NED (see Table 5).
[a] Units are $\times 10^{-3}$counts s^{-1}.
[b] Units are $\times 10^{44}$ erg s^{-1}.

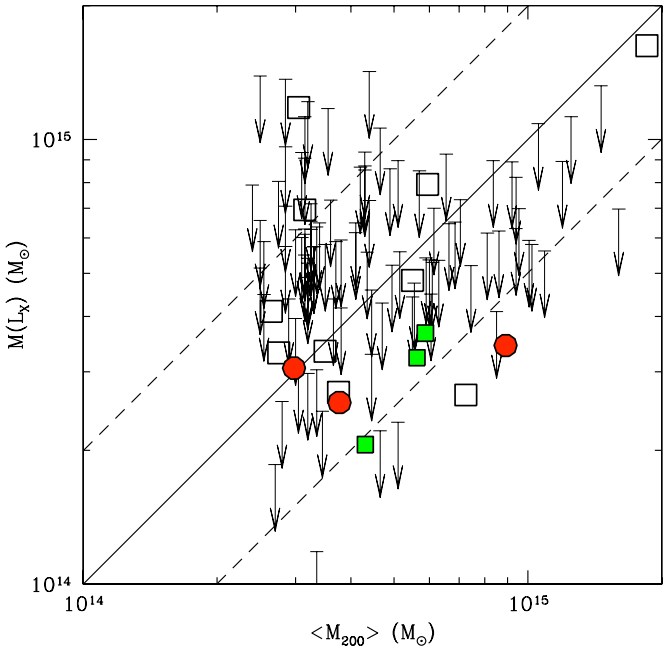

Figure 6. Plot of X-ray vs. optically derived masses for all SCS clusters. The optical mass is the average of $M(N_{200})$ and $M(L_{200})$, while the X-ray mass comes from the X-ray luminosity assuming an M–L_X scaling relation. Clusters with X-ray emission are shown as the box symbols, while the others are shown as upper limits. The solid line denotes equality; the dashed lines indicate a factor of two range in mass. The green points show the average optical and X-ray masses for clusters stacked in three redshift bins (0.0–0.4, 0.4–0.6, and 0.6–0.8) ordered from bottom to top, while the red points are stacked in three optical mass bins ($<3.2 \times 10^{14}$ $M_\odot$, 3.2×10^{14} $M_\odot$ to 4.5×10^{14} $M_\odot$, and $>4.5 \times 10^{14}$ $M_\odot$) ordered from left to right.

(A color version of this figure is available in the online journal.)

instrumental response functions (i.e., the arf and rmf files) for each cluster. X-ray luminosity values were determined using the extracted spectra and response files assuming a simple source emission model consisting of an absorbed thermal plasma model. For the absorption component we fixed the column density of neutral hydrogen to the Galactic value toward the cluster position (obtained in the same way as for the RASS discussed above). Three clusters have enough signal that their mean temperatures can be measured (see below); for the others we assume $kT = 5$ keV for the luminosity calculation. The final column lists the cluster mass inferred from the X-ray luminosity as discussed above.

The *XMM-Newton* spectra constrain the cluster temperatures for SCSO J051558−543906 and SCSO J231651−545356 to values of $kT = 1.8^{+0.5}_{-0.3}$ keV and $kT = 3.7^{+0.6}_{-0.5}$ keV, respectively (errors are at the 68% confidence interval), assuming a metal abundance of 0.3 times the solar value. SCSO J051637−543001 (Abell S0520) is a bright cluster that was the target of a specific *XMM-Newton* program. Our analysis finds a best fit temperature of $kT = 7.7 \pm 0.3$ keV and a metal abundance of 0.17 ± 0.04 relative to solar, which are both consistent with previous work (e.g., Zhang et al. 2006). The X-ray masses for these three systems just mentioned agree quite well with the optically derived masses and, in the case of SCSO J051637−543001, with the *ROSAT*-derived mass as well. For the three other clusters in the 23 hr region in Table 7, the X-ray masses are all lower than the optical masses by factors of 3–5. For the remaining system (SCSO J051613−542620), there is a catastrophic disagreement between the inferred optical and X-ray masses with the X-ray mass being more than an order of magnitude below the optical one. This is likely due to significant contamination of the optical number counts by cluster members from the nearby, rich system Abell S0520 which is also close in redshift (0.2952 versus 0.36).

4. SUMMARY

We have fully processed using an independent custom-built pipeline ∼1 TB of archival *griz* imaging data from the CTIO Blanco 4 m telescope acquired under the NOAO Large Survey program (05B-0043, PI: Joe Mohr), as part of our own SCS. This data volume corresponds to 45 nights of observing over 3 years (2005–2007) and covers 70 deg^2 of the southern sky that has also been fully observed by ACT and SPT. Here, we have presented the first results from the full nominal data set, namely, a sample of 105 massive, optically selected galaxy clusters. Future studies will present the properties of lower mass clusters and groups as well as multi-wavelength studies of cluster physics utilizing selected clusters from this sample.

The current sample is limited to systems with optically derived masses greater than 3×10^{14} $M_\odot$ and redshifts less than 0.8. We have chosen this mass limit to be at or below the anticipated mass threshold of ACT and SPT in order to encompass the upcoming significant SZE detections. However, we also have a redshift limit which is due to the depth of the imaging and the wavelength coverage of the filter set. Thus, we are missing the most interesting massive clusters at high redshift ($z > 0.8$). However, as demonstrated in Menanteau & Hughes

(2009), the optical data analyzed here can be used to confirm the presence of a cluster when conducting a targeted positional search for a high significance SZE candidate.

The recent success of the millimeter-band wide-survey-area experiments (ACT and SPT) in finding new clusters through untargeted SZE surveys has been a strong catalyst for our work. We present this cluster sample to aid in the verification of SZE cluster candidates and the characterization of the SZE selection function which currently is observationally unexplored. Moreover, we anticipate stacking the ACT millimeter-band maps at the positions of optical clusters to detect, statistically, the average SZE signal for systems that fall below the ACT detection threshold for individual sources.

Given the large volume of this data set we believe it might be helpful to address other problems in astrophysics; therefore, we plan to make the Blanco data products (i.e., photometric source catalogs and images) available to the community in 2010 December at the following URL http://scs.rutgers.edu.

We thank the Blanco Cosmology Survey team for the planning and execution of the CTIO Blanco observations that were used in this paper. We have made use of the *ROSAT* Data Archive of the Max-Planck-Institut für extraterrestrische Physik (MPE) at Garching, Germany as well as results obtained from the High Energy Astrophysics Science Archive Research Center, provided by NASA's Goddard Space Flight Center. This research has made use of data obtained from or software provided by the US National Virtual Observatory, which is sponsored by the National Science Foundation. This research has made use of the NASA/IPAC Extragalactic Database (NED) which is operated by the Jet Propulsion Laboratory, California Institute of Technology, under contract with the National Aeronautics and Space Administration. Partial financial support was provided by the National Science Foundation under the PIRE program (award number OISE-0530095). We also acknowledge support from NASA/XMM grants NNX08AX55G and NNX08AX72G.

REFERENCES

Abell, G. O. 1958, ApJS, 3, 211
Abell, G. O., Corwin, H. G., Jr., & Olowin, R. P. 1989, ApJS, 70, 1
Annis, J., et al. 1999, BAAS, 31, 1391
Becker, M. R., et al. 2007, ApJ, 669, 905
Benítez, N. 2000, ApJ, 536, 571
Bertin, E. 2006, SWarp Resample and Coadd Software, http://terapix.iap.fr/cplt/oldSite/soft/swarp/index.html
Bertin, E., & Arnouts, S. 1996, A&AS, 117, 393
Blakeslee, J. P., et al. 2003, ApJ, 596, L143
Blanton, M. R., et al. 2003, ApJ, 592, 819
Bower, R. G., Lucey, J. R., & Ellis, R. S. 1992, MNRAS, 254, 601
Dong, F., Pierpaoli, E., Gunn, J. E., & Wechsler, R. H. 2008, ApJ, 676, 868
Fowler, J. W., et al. 2010, ApJ, 722, 1148
Gal, R. R. 2008, in A Pan-Chromatic View of Clusters of Galaxies and the Large-Scale Structure, ed. M. Plionis, O. Lpez-Cruz, & D. Hughes (Lecture Notes in Physics, Vol. 740; Dordrecht: Springer), 119
Gal, R. R., de Carvalho, R. R., Odewahn, S. C., Djorgovski, S. G., & Margoniner, V. E. 2000, AJ, 119, 12
Gal, R. R., Lopes, P. A. A., de Carvalho, R. R., Kohl-Moreira, J. L., Capelato, H. V., & Djorgovski, S. G. 2009, AJ, 137, 2981
Gladders, M. D., Hoekstra, H., Yee, H. K. C., Hall, P. B., & Barrientos, L. F. 2003, ApJ, 593, 48
Gladders, M. D., & Yee, H. K. C. 2000, AJ, 120, 2148
Gladders, M. D., & Yee, H. K. C. 2005, ApJS, 157, 1
Goto, T., et al. 2002, AJ, 123, 1807
Hansen, S. M., McKay, T. A., Wechsler, R. H., Annis, J., Sheldon, E. S., & Kimball, A. 2005, ApJ, 633, 122
Hincks, A. D., et al. 2009, arXiv:0907.0461
Johnston, D. E., et al. 2007, arXiv:0709.1159
Kalberla, P. M. W., Burton, W. B., Hartmann, D., Arnal, E. M., Bajaja, E., Morras, R., & Pöppel, W. G. L. 2005, A&A, 440, 775
Koester, B. P., et al. 2007a, ApJ, 660, 221
Koester, B. P., et al. 2007b, ApJ, 660, 239
Komatsu, E., et al. 2010, arXiv:1001.4538
Kravtsov, A. V., Vikhlinin, A., & Nagai, D. 2006, ApJ, 650, 128
Loh, Y.-S., & Strauss, M. A. 2006, MNRAS, 366, 373
Lopes, P. A. A., de Carvalho, R. R., Gal, R. R., Djorgovski, S. G., Odewahn, S. C., Mahabal, A. A., & Brunner, R. J. 2004, AJ, 128, 1017
Lueker, M., et al. 2010, ApJ, 719, 1045
Mauch, T., Murphy, T., Buttery, H. J., Curran, J., Hunstead, R. W., Piestrzynski, B., Robertson, J. G., & Sadler, E. M. 2003, MNRAS, 342, 1117
McInnes, R. N., Menanteau, F., Heavens, A. F., Hughes, J. P., Jimenez, R., Massey, R., Simon, P., & Taylor, A. 2009, MNRAS, 399, L84
Menanteau, F., & Hughes, J. P. 2009, ApJ, 694, L136
Menanteau, F., et al. 2009, ApJ, 698, 1221
Okabe, N., Takada, M., Umetsu, K., Futamase, T., & Smith, G. P. 2010, PASJ, 62, 811
Postman, M., Lubin, L. M., Gunn, J. E., Oke, J. B., Hoessel, J. G., Schneider, D. P., & Christensen, J. A. 1996, AJ, 111, 615
Ramella, M., Boschin, W., Fadda, D., & Nonino, M. 2001, A&A, 368, 776
Reiprich, T. H., & Böhringer, H. 2002, ApJ, 567, 716
Reyes, R., Mandelbaum, R., Hirata, C., Bahcall, N., & Seljak, U. 2008, MNRAS, 390, 1157
Rozo, E., et al. 2009a, ApJ, 703, 601
Rozo, E., et al. 2009b, ApJ, 699, 768
Rozo, E., et al. 2010, ApJ, 708, 645
Rykoff, E. S., et al. 2008, MNRAS, 387, L28
Schlegel, D. J., Finkbeiner, D. P., & Davis, M. 1998, ApJ, 500, 525
Sheldon, E. S., et al. 2009, ApJ, 703, 2217
Skrutskie, M. F., et al. 2006, AJ, 131, 1163
Smith, J. A., Allam, S. S., Tucker, D. L., Stute, J. L., Rodgers, C. T., & Stoughton, C. 2007, AJ, submitted
Staniszewski, Z., et al. 2009, ApJ, 701, 32
Sunyaev, R. A., & Zel'dovich, Y. B. 1972, Comments Astrophys. Space Phys., 4, 173
Valdes, F. G. 1998, in ASP Conf. Ser. 145, Astronomical Data Analysis Software and Systems VII, ed. R. Albrecht, R. N. Hook, & H. A. Bushouse (San Francisco, CA: ASP), 53
Vikhlinin, A., et al. 2009, ApJ, 692, 1033
Voges, W., et al. 1999, A&A, 349, 389
Zhang, Y.-Y., Böhringer, H., Finoguenov, A., Ikebe, Y., Matsushita, K., Schuecker, P., Guzzo, L., & Collins, C. A. 2006, A&A, 456, 55